Extracting near-field seismograms from ocean-bottom pressure gauge inside the focal area: application to the 2011 Mw 9.1 Tohoku-Oki earthquake

T. Kubota[1], T. Saito[1], H. Tsushima[2], R. Hino[3], Y. Ohta[3], S. Suzuki[3], D. Inazu[4]

[1] National Research Institute for Earth Science and Disaster Resilience, Tsukuba, Japan

[2] Meteorological Research Institute, Japan Meteorological Agency, Tsukuba, Japan

[3] Graduate School of Science, Tohoku University, Sendai, Japan

[4] Department of Marine Resources and Energy, Tokyo University of Marine Science and Technology, Tokyo, Japan

Corresponding author: Tatsuya Kubota (kubotatsu@bosai.go.jp)

Key Points:

- We develop a method to extract low-frequency ground motion including permanent deformation from ocean-bottom pressure gauge (OBP) data
- We obtain the seismograms inside the focal area of the 2011 Tohoku-Oki EQ, which suggest two dominant energy releases around the hypocenter
- High-frequency near-field OBP signals should be utilized more widely for geophysical research as well as real-time tsunami forecasting

Abstract

Recent studies have shown that ocean-bottom pressure gauges (OBPs) can record seismic waves in addition to tsunamis and seafloor permanent displacements, even if they are installed inside the focal area where the signals are extremely large. We developed a method to extract dynamic ground motion waveforms from near-field OBP data consisting of a complex mixture of various signals, based on an inversion analysis along with a theory of tsunami generation. We applied this method to the OBP data of the 2011 Tohoku-Oki earthquake. We successfully extracted the low-frequency vertical seismograms inside the focal area ($f < \sim 0.05$ Hz), although those of the Mw ~9 megathrust earthquake had never previously been reported. The seismograms suggested two dominant energy releases around the hypocenter. The seismic wave signals recorded by the near-field OBP will be important not only to reveal earthquake ruptures and tsunami generation processes but also to conduct real-time tsunami forecasts.

Plain Language Summary

During tsunami generation, different types of waves such as ground motions, ocean acoustic waves, and tsunamis coexist inside the focal area, forming complicated wavefields and pressure changes at the sea bottom. This study developed a method to appropriately decompose the complicated ocean-bottom pressure gauge (OBP) waveforms into ground motion and tsunami signals. Our method was applied to the near-field OBP data of the 2011 Tohoku-Oki earthquake to extract the near-field seismic motion waveform which had never been reported previously. The waveform suggested a complex earthquake rupture process along the plate boundary, in which the rupture happened twice near the hypocenter. The seismic wave signals recorded by the near-field OBP will be important not only to reveal the processes of the earthquake rupture and tsunami generation but also to issue tsunami alarms.

1 Introduction

Seismic observations are very important to estimate earthquake source parameters and physical properties around the fault and to understand how an earthquake plays a role in geodynamic frameworks. Far-field seismograms have been used for earthquake kinematic rupture modeling (e.g., Lay et al., 2011). Near-field seismograms are also essential to resolve the rupture kinematics, because far-field seismograms are affected by path effects such as attenuation and scattering and resolve very little about the short-wavelength information on the source (e.g., Aki & Richards, 2002). Near-fault seismograms are also important for earthquake rupture dynamics. Stress drop, defined as shear stress reduction on the fault due to an earthquake, and slip weakening distance Dc, the slip amount needed to reach residual friction, are often inferred from near-field seismograms (e.g., Ide & Takeo, 1997; Mikumo et al., 2003; Fukuyama & Mikumo, 2007; Fukuyama & Suzuki, 2016; Kaneko et al., 2017).

In the 2011 Tohoku-Oki earthquake (Mw 9.1, Global Centroid Moment Tensor [GCMT]; hereafter, the mainshock), various near-field observations were recorded, which were not obtained for past megathrust earthquakes (e.g., Hino, 2015; Lay, 2018; Wang et al., 2018; Kodaira et al., 2020). Seafloor geodetic observations (e.g., Fujiwara et al., 2011; 2017; Ito et al., 2011; Kido et al., 2011; Sato et al., 2011) have particularly played an important role in revealing the mainshock rupture process and tsunami generation (e.g., Iinuma et al., 2012). However, near-field seismograms associated with the mainshock with a reasonable quality have not been reported. The high-sensitivity ocean-bottom seismometers (OBSs) installed off Miyagi (Suzuki et al., 2012) went off-scale and whole seismograms were not recorded. The strong motion accelerometers installed outside of the main rupture area (open triangles in Figure 1a) were dynamically rotated by the strong shaking (Nakamura & Hayashimoto, 2019). Although some near-source seismograms during past megathrust earthquakes have been recorded by onshore seismometers and GNSS, such as in the 2010 and 2014 Chile earthquakes (Vigny et al., 2011; Madariaga et al., 2019), the stations were located outside of the main rupture regions, where the permanent displacement was small.

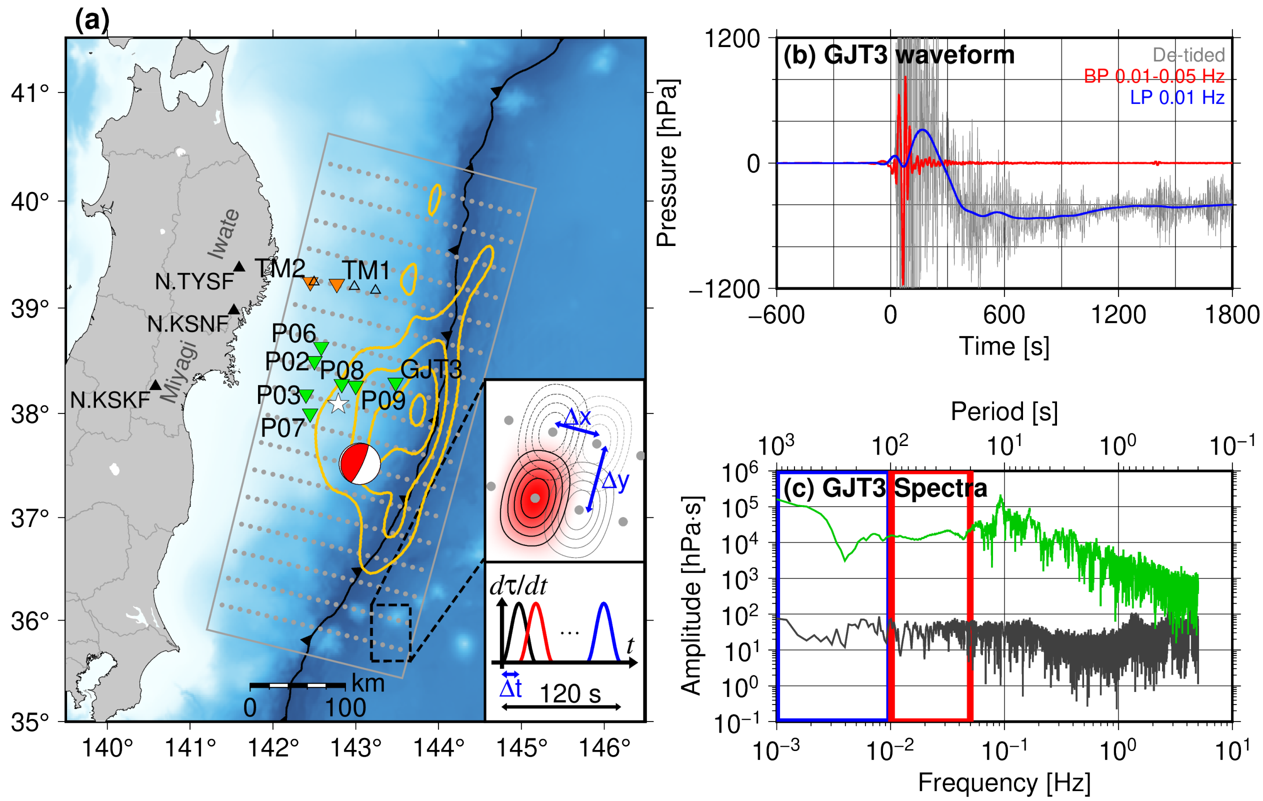

Figure 1. (a) Location map of this study. Inverted triangles denote OBPs (green: Tohoku University, orange: ERI). Open triangles denote OBS stations by ERI. Black triangles are the F-net onshore seismometers. The white star is the mainshock epicenter (Suzuki et al., 2012) and the red CMT solution is taken from GCMT. Yellow contours denote the distributions of the initial tsunami height (Saito et al., 2011, 2 m interval). Gray dots and rectangular areas indicate the locations of the unit sources and the analytical area of the inversion analysis. The configuration of the unit sources in the space and time domains is schematically shown in the inset. (b) Pressure waveforms at GJT3. Gray, red, and blue traces are the de-tided, bandpass filtered (0.01–0.05 Hz), and lowpass filtered (0.01 Hz) waveforms, respectively. (c) Spectral amplitude before and after the mainshock (black and green, respectively), calculated based on Aki and Richards' (2002) definition. Passbands of the filters in Figure 1b are marked by colored rectangles.

During the mainshock, some ocean-bottom pressure gauges (OBPs) were installed around the main rupture area (inverted triangles in Figure 1). The deep-ocean OBPs often observe tsunamis, which have dominant frequencies lower than ~0.01 Hz. Such tsunami data have been widely utilized, because tsunamis constrain the spatial extent of the seafloor vertical deformation (tsunami source) better than seismic waves (Kubota et al., 2018). This is attributed to tsunamis' much slower propagation velocity and there being a less significant tradeoff between the source dimension and rupture propagation velocity across the fault. Previous studies used the mainshock OBP data to investigate the mainshock tsunami generation process (e.g., Saito et al., 2011 (yellow contour lines in Figure 1a); Maeda et al., 2011; Tsushima et al., 2011; Gusman et al., 2012; Satake et al., 2013; Baba et al., 2015; Hossen et al., 2015; Dettmer et al., 2016; Yamazaki et al., 2018). However, they did not utilize the OBPs installed inside the main tsunami source region where the seafloor uplift was extremely large (e.g., GJT3, Figure 1). This is mainly because there have been few near-field observation examples (e.g., Mikada et al., 2006) and the method to utilize the permanent deformation for tsunami modeling was not established. In this decade, the well-established method to utilize the permanent deformation for tsunami modeling was proposed (Tsushima et al., 2012) and many finite fault models using the OBPs inside the tsunami source have been obtained (e.g., Kubota, Hino et al., 2017; Nemoto et al., 2019).

Our understanding of the ocean-bottom pressure change inside the focal area during tsunami generation has also progressed. The three-dimensional theory based on the tsunami generation mechanics showed the initial sea-surface distribution is not identical to the seafloor elevation (e.g., Kajiura, 1963; Saito & Furumura, 2009). Based on the three-dimensional theory, the pressure change inside the focal area includes a component related to vertically accelerating seafloor (Filloux, 1982; Saito, 2013; 2017; 2019; An et al., 2017). This component was confirmed by the actual observations and numerical simulations (e.g., Filloux, 1982; Webb, 1998; Nosov and Kolesov, 2007; Matsumoto et al., 2012; 2017; Saito & Tsushima, 2016; An et al., 2017; Kubota, Saito et al., 2017; Saito, 2019; Ito et al., 2020; Mizutani et al., 2020; Saito & Kubota, 2020; Kubota et al., 2020). Additionally, the pressure change field includes the high-frequency ocean-acoustic waves related to the seawater elasticity (Nozov & Kolesov, 2007, Saito & Tsushima, 2016; Lotto et al., 2018). Recently the attempts to numerically simulate this complex pressure change field have started (e.g., Lotto et al., 2015; Saito et al., 2019; Abrahams et al., 2020; Maeda et al., 2020). However, although the method to forwardly simulate more realistic OBP signals inside the focal has been established, it has also been reported that a simple bandpass filter cannot extract the seismic waves from the complex pressure change field (Saito & Tsushima, 2016). A method to appropriately decompose the OBP signal to the seismic and tsunami signals is not established yet.

The purpose of this study is to propose a method to appropriately extract the seafloor dynamic motion time series from the near-field OBP data inside the focal area. To achieve this, we attempt to decompose the OBP signals into seismic and tsunami wave signals based on a tsunami generation theory. Section 2 describes a theory of tsunami generation inside the focal area, the mainshock OBP data used in this study, and the procedure of our method. In section 3, we show the results of the application of the method to the mainshock OBP data. Discussion and summary of this study are given in sections 4 and 5, respectively.

2 Data and Methods

2.1 Ocean-bottom pressure inside the focal area

We represent the ocean-bottom pressure change inside the focal area as the sum of the contribution originating due to gravity ($p_{\mathrm{gravity}}(t)$) and that without gravity $p_{\mathrm{non-gravity}}(t)$

(Saito, 2019):

$$p(t) = p_{\mathrm{gravity}}(t) + p_{\mathrm{non-gravity}}(t). \quad (1)$$

Supposing that the wave period is long, we may consider the seawater as an incompressible fluid. Also supposing that the sea-surface height change is small enough compared to the water depth and that the wavelength is much longer than the sea depth, $p_{\mathrm{gravity}}(t)$ is approximately given by

$$p_{\mathrm{gravity}}(t) \approx p_{\mathrm{hydrostatic}}(t) = \rho_0 g_0[\eta(t) - u_z(t)], \quad (2)$$

where $\rho_0 = 1030\ \mathrm{kg/m^3}$ and $g_0 = 9.8\ \mathrm{m/s^2}$ are the seawater density and gravity acceleration, and $\eta(t)$ and $u_z(t)$ are the time series of the sea-surface height change (tsunami) and the seafloor vertically upward displacement, respectively. Hereinafter we refer to $p_{\mathrm{hydrostatic}}(t)$ as the hydrostatic pressure change. The pressure change without gravity can be approximated as the dynamic pressure change, related to the action-reaction forces of the vertically accelerating seafloor, as (e.g., Saito, 2013; Saito & Kubota, 2019)

$$p_{\mathrm{non-gravity}}(t) \approx p_{\mathrm{dynamic}}(t) = \rho_0 h_0 \frac{d^2 u_z(t)}{dt^2}, \quad (3)$$

where h_0 is seawater depth. This relationship is basically valid at frequencies lower than the acoustic resonant frequency: $f_0 = c_0/4h_0$ ~ 0.05 Hz (c_0: ocean-acoustic wave velocity). In this study, we attempt to extract the vertical acceleration d^2u_z/dt^2 from the pressure change $p(t)$.

2.2 OBP data

We use seven OBPs installed off Miyagi (green inverted triangles in Figure 1a, Hino et al., 2014) and two OBPs installed off Iwate (orange inverted triangles, Kanazawa & Hasegawa, 1997; Maeda et al., 2011). See Text S1 for the detail of these instruments. Station locations are listed in Table S1. We subtract the tidal components using the model of Matsumoto et al. (2000). We then apply a 4th-order Butterworth lowpass filter with a cutoff of 0.05 Hz in both forward and backward directions to reduce higher-frequency ocean-acoustic wave components. The cutoff of 0.05 Hz is determined considering the acoustic resonant frequency f_0 for the OBP at GJT3 (~ 0.11 Hz). All records are resampled to 1 Hz after the filtering.

The de-tided waveform at GJT3 is shown in Figure 1b (gray trace). In Figure 1c, spectral amplitudes of the de-tided records before and after the mainshock are shown, which are calculated based on Aki and Richards' (2002) definition (time windows of 3276.8 s are used). High-frequency ocean-acoustic wave signals can be recognized even 1800 s after the origin time, and are dominant in frequencies higher than the acoustic resonant frequency f_0 ~0.11 Hz.

Dynamic pressure changes (Eq. (3)) are evident during the first few minutes, particularly for the frequency range 0.01–0.05 Hz (red traces in Figure 1b). Subsequently, low-frequency hydrostatic pressure changes (Eq. (2)) are also confirmed (< 0.01 Hz, blue).

2.3 Extracting ground motions from OBP data

This study attempts to extract the vertical acceleration d^2u_z/dt^2 in Eq. (3) from the OBP data. In other words, our goal is to appropriately decompose the observed pressure change into its hydrostatic and dynamic components. To achieve this, we develop a method based on the inversion for the temporal evolution of the seafloor vertical deformation combined with the theory for ocean-bottom pressure inside the focal area described in section 2.1. We represent the vertical displacement at the seafloor ($u_z(x,y,t)$) by the superposition of functions $U_{z,ij}$ and τ_k,

$$u_z(x,y,t) = \sum_{i=1}^{N_x}\sum_{j=1}^{N_y}\sum_{k=1}^{N_t} m_{ijk} U_{z,ij}(x,y)\tau_k(t). \tag{5}$$

The basis function for the spatial distribution of the seafloor vertical displacement $U_{z,ij}(x,y)$ is given by

$$U_{z,ij}(x,y) = \left[\frac{1}{2}+\frac{1}{2}\cos\left(\frac{2\pi(x-x_i)}{L_x}\right)\right]\left[\frac{1}{2}+\frac{1}{2}\cos\left(\frac{2\pi(y-y_j)}{L_y}\right)\right]$$
$$\text{for} \quad x_i-\frac{L_x}{2} \le x \le x_i+\frac{L_x}{2},\ y_j-\frac{L_y}{2} \le y \le y_j+\frac{L_y}{2}, \tag{6}$$

which takes the maximum value at (x_i, y_j). The displacement time function $\tau_k(t)$ is given by

$$\tau_k(t) = \begin{cases} 0 & \text{for } t \le t_k \\ \frac{1}{T_\mathrm{d}}\left[t - \frac{T_\mathrm{d}}{2\pi}\sin\left(\frac{2\pi(t-t_k)}{T_\mathrm{d}}\right)\right] & \text{for } t_k \le t \le t_k + T_\mathrm{d}, \\ 1 & \text{for } t_k + T_\mathrm{d} \le t \end{cases} \tag{7}$$

where the function begins to increase at $t = t_k$ and reaches 1 after the duration T_d. The coefficient m_{ijk} in Eq. (5) represents the displacement amplitude of the (i,j,k)-th function $U_{z,ij}(x,y)\tau_k(t)$.

The hydrostatic pressure change at the n-th OBP located at (x_n, y_n) is given by

$$p_\mathrm{hydrostatic}(x_n,y_n,t) = \rho_0 g_0[\eta(x_n,y_n,t) - u_z(x_n,y_n,t)]. \tag{8}$$

The first and second terms represent the pressure changes due to the tsunami and the vertical displacement at the seafloor at (x_n, y_n), respectively. The tsunami height $\eta(x,y,t)$ is numerically calculated by solving the linear tsunami equation from the seafloor vertical displacement $u_z(x, y, t)$ (Eq. (5)). Since the $p_{\mathrm{hydrostatic}}(x_n, y_n, t)$ is linear with respect to the seafloor displacement, we represent Eq. (9) as the superposition using m_{ijk}:

$$p_{\mathrm{hydrostatic}}(x_n, y_n, t) = \sum_{i=1}^{N_x} \sum_{j=1}^{N_y} \sum_{k=1}^{N_t} m_{ijk} G_{ijk,n}^{\mathrm{hydrostatic}}(x_n, y_n, t). \tag{10}$$

We refer to $G_{ijk,n}^{\mathrm{hydrostatic}}(x, y, t)$ as the hydrostatic pressure Green's function in this study, which is the hydrostatic pressure change at (x, y) excited by the unit vertical displacement of $U_{z,ij}(x, y)\tau_k(t)$.

The dynamic pressure change at the n-th OBP located at (x_n, y_n) (Eq. (3)) is given by the displacement of Eq. (5):

$$\begin{aligned} p_{\mathrm{dynamic}}(x_n, y_n, t) &= \rho_0 h_0 \frac{\partial^2 u_z(x_n, y_n, t)}{\partial t^2} \\ &= \rho_0 h_0 \sum_{i=1}^{N_x} \sum_{j=1}^{N_y} \sum_{k=1}^{N_t} m_{ijk} U_{z,ij}(x_n, y_n) \frac{\partial^2 \tau_k(t)}{\partial t^2} \\ &= \sum_{i=1}^{N_x} \sum_{j=1}^{N_y} \sum_{k=1}^{N_t} m_{ijk} G_{ijk,n}^{\mathrm{dynamic}}(x_n, y_n, t), \end{aligned} \tag{11}$$

where

$$\frac{\partial^2 \tau_k(t)}{\partial t^2} = \begin{cases} 0 & \text{for } t \le t_k, t_k + T_{\mathrm{d}} \le t \\ \frac{2\pi}{T_{\mathrm{d}}^2} \sin\left(\frac{2\pi(t - t_k)}{T_{\mathrm{d}}}\right) & \text{for } t_k \le t \le t_k + T_{\mathrm{d}} \end{cases}. \tag{12}$$

We refer to $G_{ijk,n}^{\mathrm{dynamic}}(x, y, t)$ as the dynamic pressure Green's function, which represents the dynamic pressure change at (x, y) excited by the unit vertical displacement of $U_{z,ij}(x, y)\tau_k(t)$.

By using Eqs. (10) and (11), we represent the pressure change at the n-th OBP excited by the vertical seafloor motions as

$$\begin{aligned} p(x_n, y_n, t) &= \sum_{i=1}^{N_x} \sum_{j=1}^{N_y} \sum_{k=1}^{N_t} m_{ijk} \left[G_{ijk,n}^{\mathrm{hydrostatic}}(x_n, y_n, t) + G_{ijk,n}^{\mathrm{dynamic}}(x_n, y_n, t) \right] \\ &= \sum_{i=1}^{N_x} \sum_{j=1}^{N_y} \sum_{k=1}^{N_t} m_{ijk} G_{ijk}(x_n, y_n, t), \end{aligned} \tag{13}$$

where the Green's function $G_{ijk}(x, y, t)$ is given by

$$G_{ijk}(x, y, t) = G_{ijk}^{\mathrm{hydrostatic}}(x, y, t) + G_{ijk}^{\mathrm{dynamic}}(x, y, t), \tag{14}$$

which represents the pressure change at (x, y) excited by the unit vertical displacement of $U_{z,ij}(x, y)\tau_k(t)$.

We estimate the displacement amplitude m_{ijk} as model parameters in a linear inversion problem given by Eq. (13), where the pressure change at the n-th OBP is used as the data. Using the estimated m_{ijk} with Eqs. (10) and (11), the observed pressure change at the n-th OBP can be decomposed into the hydrostatic and dynamic components. The time history of the vertical acceleration can also be extracted using Eq. (11), as

$$\frac{\partial^2 u_z(x_n, y_n, t)}{\partial t^2} = \frac{1}{\rho_0 h_0} \sum_{i=1}^{N_x} \sum_{j=1}^{N_y} \sum_{k=1}^{N_t} m_{ijk} G_{ijk,n}^{\text{dynamic}}(x_n, y_n, t)$$

$$= \sum_{i=1}^{N_x} \sum_{j=1}^{N_y} \sum_{k=1}^{N_t} m_{ijk} U_{z,ij}(x_n, y_n) \frac{\partial^2 \tau_k(t)}{\partial t^2}. \quad (15)$$

In the same manner, vertical velocity and displacement can also be obtained. For example, vertical velocity is expressed as

$$\frac{\partial u_z(x_n, y_n, t)}{\partial t} = \sum_{i=1}^{N_x} \sum_{j=1}^{N_y} \sum_{k=1}^{N_t} m_{ijk} U_{z,ij}(x_n, y_n) \frac{\partial \tau_k(t)}{\partial t} \quad (16)$$

where

$$\frac{\partial \tau_k(t)}{\partial t} = \begin{cases} 0 & \text{for } t \le t_k, t_k + T_\mathrm{d} \le t \\ \frac{1}{T_\mathrm{d}}\left[1 - \cos\left(\frac{2\pi(t - t_k)}{T_\mathrm{d}}\right)\right] & \text{for } t_k \le t \le t_k + T_\mathrm{d} \end{cases}. \quad (17)$$

2.4 Calculation of Green's function and inversion

We summarize the procedures of the Green's function calculation and the inversion analysis (see Text S2 for more detail). We suppose the x- and y-directions are along the trench-normal and trench-parallel directions, respectively. We distribute the spatial basis function $U_{z,ij}$ in an area of 220 km × 270 km (gray dots in Figure 1a). We suppose the elliptical-shaped unit sources to be $L_x = 20$ km and $L_y = 60$ km and each of them overlaps with their adjacent ones (inset of Figure 1a). We also distribute the temporal basis functions τ_k with the temporal interval of $\Delta t = 5$ s, during the 120 s from the origin time (inset of Figure 1a). Duration of τ_k is assumed as $T_\mathrm{d} = 10$ s. To calculate the hydrostatic Green's function, tsunami height is numerically simulated from the initial tsunami height distribution using the linear dispersive tsunami equation (e.g., Saito, 2019). We use the bathymetry data of GEBCO Bathymetric Compilation Group (2020), decimating to a spatial grid interval of 2 km. The input sea-surface height for the tsunami calculation is calculated from the unit seafloor displacement with the water wave theory assuming a constant depth of 6 km (Kajiura, 1963). The dynamic Green's functions are calculated, using the seawater depth h_0 for each station (Table S1). After the calculation of the Green's functions, the same filter as applied to the observation is also applied to the Green's functions.

In the inversion, we impose the constraints of the spatial smoothing (Baba et al., 2006) and spatial damping. The weights of each constraint are determined based on trial and error. The deformations are allowed to begin at $t = 0$ s. We use 3600-s time windows for the OBPs off Miyagi and 1800-s for the OBPs off Iwate.

3 Results

In Figure 2a, we compare the observed pressure changes at GJT3 with the synthesized ones (see Figure S1 for the other OBPs, Figures S2 and S3 for the spatial distribution of the total displacement and its temporal evolution). Figure 2b shows the extracted vertical accelerograms at the OBPs using the estimated model parameter m_{ijk} in Eq. (12). Compared to the observed pressure changes divided by $\rho_0 h_0$ (black traces), the extracted accelerograms (red traces) do not contain the low-frequency pressure signals due to the tsunami, which are evident after ~120 s from the origin time. High-frequency pressure changes for the first 120 s are explained by the dynamic pressure components (green trace in Figure 2a) and the subsequent low-frequency pressure changes are modeled by the hydrostatic components (blue trace), and the overall pressure changes were explained very well by both pressure changes (red trace). From the amplitude spectra of the pressure change at GJT3 (Figure S4), we confirm that the calculated hydrostatic and dynamic pressure changes are dominant only in the low- and high-frequency ranges, respectively. In Figure 2b, we also plot the accelerograms of the onshore broadband strong-motion seismometer from the F-net (Okada et al., 2004, black triangles in Figure 1a) by gray traces. Although the arrivals of the main wave packet are delayed, the onshore seismograms are similar to the extracted ocean-bottom seismograms at the OBPs near each station (compare N.TYSF with TM1 and TM2, N.KSNF with P02 and P06, and N.KSKF with P03 and P07). We also show the vertical velocity and displacement waveforms in Figures 3a and 3b, respectively. The amounts of the calculated vertical displacements are surprisingly consistent with the observed pressure offset changes due to the permanent deformation (Figure 3c, Figure S5 shows comparisons for longer time window). These comparisons indicate the validity of the extracted seismograms.

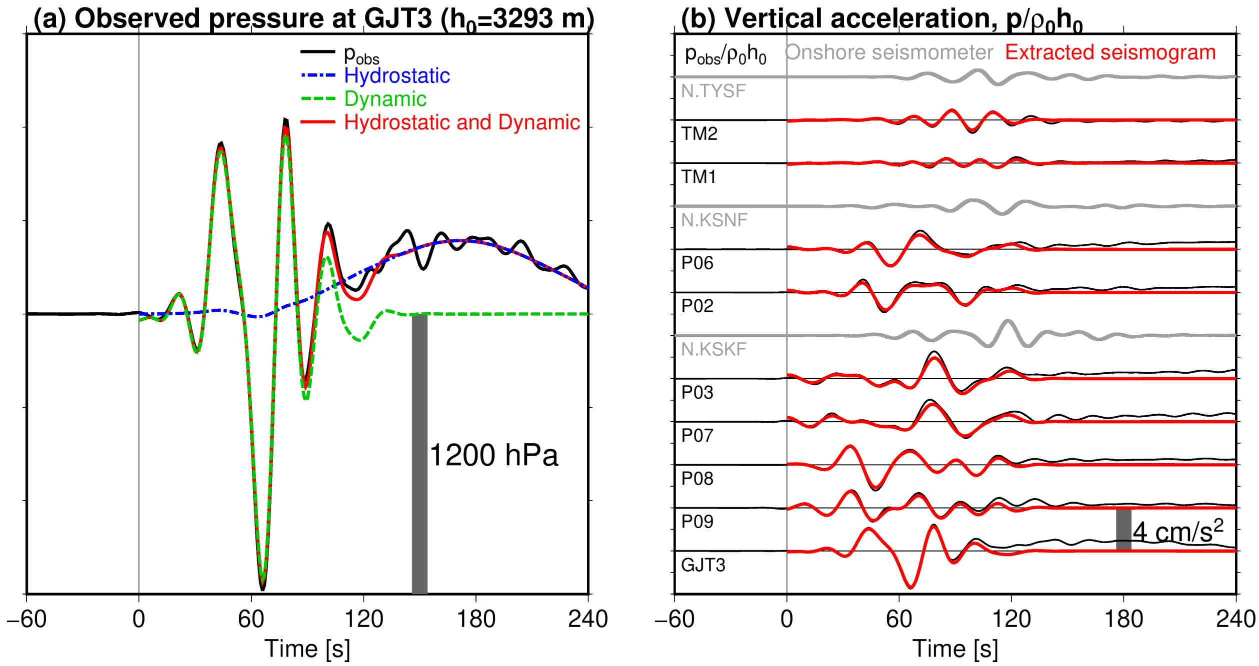

Figure 2. (a) Comparison of the observed OBP waveform (black) at GJT3 and the synthesized ones (blue: hydrostatic, green: dynamic, and red: both pressure changes). (b) Extracted vertical accelerograms at the OBPs (red traces). Observed pressure changes divided by $\rho_0 h_0$, which includes both tsunamis and dynamic pressure change components, are also shown by black traces. Gray traces are the observed accelerograms at the onshore seismometers.

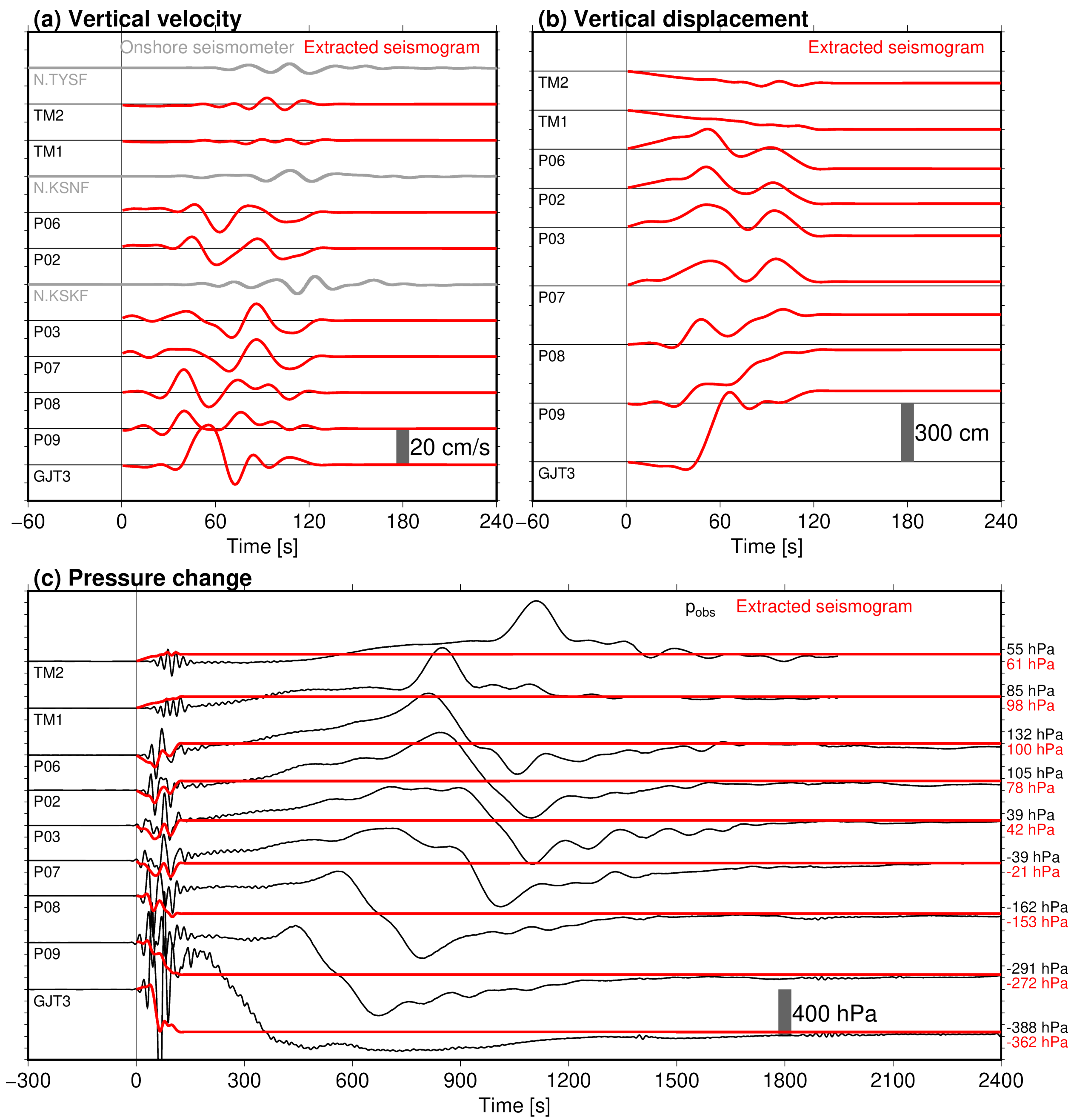

Figure 3. Time series of the extracted vertical seismograms from the OBPs (red traces), for (a) velocity and (b) displacement. Gray traces are the observed seismograms at the onshore seismometers. (c) Comparison of the observed pressure time series (black) and those expected from the extracted displacement (red). The final pressure offsets, calculated by averaging the last 600 s time window, are also shown.

It is worth pointing out that the near-field seismograms inside the tsunami source where the vertical displacement was extremely large during the Tohoku-Oki earthquake had never been reported previously. In the accelerograms at the OBPs inside the main rupture area (GJT3, P08, and P09), two dominant positive pulses are confirmed (Figure 2b). The duration of the second pulse at GJT3 is relatively short compared to the first one, whereas the durations in both pulses at P08 and P09 are similar. From the velocity seismogram at GJT3, located ~50 km landward from the trench axis, only one peak with a relatively long duration is confirmed (Figure 3a). On the other hand, at P08 and P09, located near the epicenter and ~100 km from the trench axis, there are two velocity peaks at t ~40 and ~70 s (Figure 3a). These characteristics may reflect the rupture kinematics of the mainshock. One possible interpretation is that the rupture, or energy release, at the fault beneath P08 and P09, which are located near the epicenter, occurred twice. This feature is also suggested by the kinematic modeling of the mainshock from the regional or global seismograms (Lay, 2018).

4. Discussions

This study used a lowpass filter with a cutoff of 0.05 Hz to satisfy the condition that the seawater is considered as incompressible fluid. However, if the contribution of the seawater elasticity cannot be neglected in this frequency range, the extracted seafloor seismogram may be incorrect. To confirm validity of the extracted seismograms at $f \leq 0.05$ Hz, we conduct a numerical simulation of the two-dimensional seismic wave propagation (Maeda et al., 2017, see Text S3 for the detailed settings). We assume the vertical cross-section passing through GJT3 along the trench-normal direction from the extended Japan Integrated Velocity Structure Model (Koketsu et al., 2012, top panel in Figure 4) and distribute point sources along the plate boundary. We apply lowpass filters with different cutoffs to compare the simulated pressure ($p = -\sigma_{zz}$, red traces) and the pressure-converted vertical acceleration ($\rho_0 h_0 d^2 u_z/dt^2$, blue traces) at the station GJT3. When the waveforms include high-frequency components of $f >$ ~0.1 Hz, the two waveforms are different from each other. When only focusing on the lower frequency ranges ($f \leq 0.05$ Hz), the two waveforms agree with each other. Based on this simulation, we conclude that Eq. (3) holds in the frequency range of $f \leq 0.05$ Hz, and our extracted seismograms are valid.

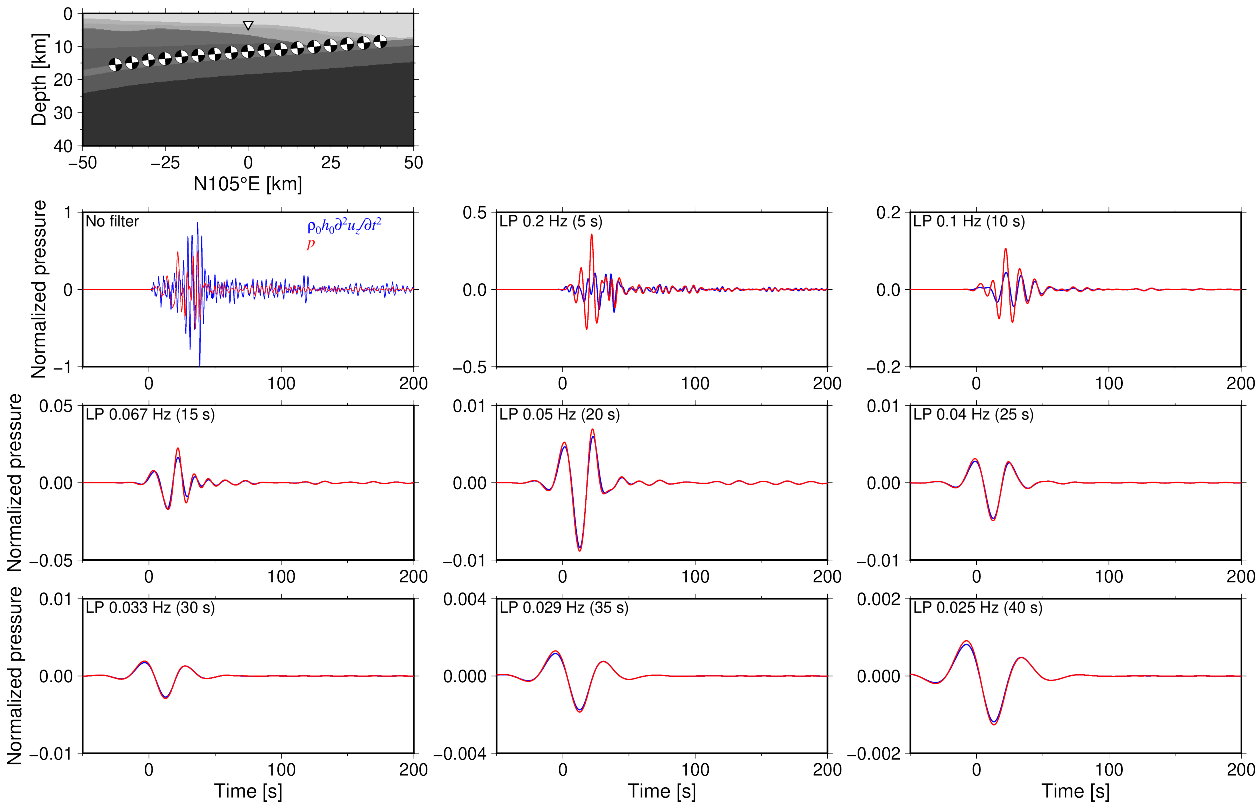

Figure 4. Result of the two-dimensional simulation of the seismic wave propagation. Structure model, point source location, and station location are shown in the top panel, and bottom panels show comparisons of the pressure-converted vertical accelerogram (blue) and the pressure waveform (red) in which lowpass filters with different cutoffs are applied.

We adopted the inversion-based method to extract the ground motion signals from the OBP data. However, one might think that the bandpass filters are also capable of extracting the seismograms by removing the low-frequency hydrostatic components. In order to evaluate this, we investigate the accelerograms calculated based on a bandpass filter with passbands of 0.01–0.05 Hz, shown in Figure S6a (black dashed line traces). The bandpass filtered accelerograms seem to agree with those extracted by our approach. However, the waveforms do not agree at all when integrating to the displacement (Figure S6b). This is because the permanent offsets are removed by the bandpass filter. Considering a slow rupture near a trench as in a tsunami earthquake (e.g., Lay et al., 2012), the megathrust earthquake rupture process possibly spans broadband frequency ranges. Because the spectral components of the mainshock ground motions possibly range into the low-frequency tsunami-dominant spectral bands, we must not use a highpass filter, which reduces the low-frequency components. It is essential to use a lowpass filter and to employ an inversion-based method with the tsunami generation theory to appropriately extract the broadband vertical ground motion including the low-frequency permanent offset component.

We could extract near-field seismograms from OBPs, which could never be achieved in the past when no OBP was installed inside the focal area and the tsunami generation theory was not established. By combining near-field OBP observation and the tsunami generation theory, it is expected that the parameters for the rupture kinematics and dynamics can be constrained more precisely, particularly for the subduction zone (e.g., Ide & Takeo, 1997; Kozdon & Dunham, 2014; Ma & Nie, 2019). In addition, developments in deep-ocean OBP observation enable us to capture the higher-frequency ocean-acoustic wave signals (Webb & Nooner, 2016; Heidarzadeh & Gusman, 2018; Kubota et al., 2020, Figure 1), which can be modeled by numerical simulation considering the seawater as the elastic body (Figure 4, Maeda et al., 2017; Saito et al., 2019). Recent studies have started to simulate pressure changes inside the focal area based on the numerical simulations, accounting for both the hydrostatic and non-hydrostatic seismic components (e.g., Saito et al., 2019; Abrahams et al., 2020; Maeda et al., 2020). Besides, in deep-ocean measurements, it is still hard to control the installation environment and some studies have reported that the near-field OBS rotated due to strong shaking on the seafloor (Nakamura & Hayashimoto, 2018; Takagi et al., 2019). In such a situation, the near-field OBPs must produce powerful datasets to constrain the earthquake source information. Taking these facts into account, the high-frequency near-field OBP data should be more utilized to deepen our geophysical understanding of the subduction zone, as widely as the data from onshore and offshore seismic instruments.

Our approach utilizing dynamic pressure may also be applicable to practical real-time tsunami early warnings (e.g., Melger & Hayes, 2019; Tsushima et al., 2011; 2012). Inside the focal area, the OBPs observe no hydrostatic pressure changes just after the origin time, because the sea-surface height change and seafloor vertical displacement are almost equivalent soon after the earthquake occurrence (Tsushima et al., 2012). If we utilize the dynamic pressure changes as vertical motion signals, which are dominant in the first few minutes, the accuracy of the tsunami forecast immediately after the earthquake rupture starts will be improved. In Figure S7, we apply the bandpass filter to the extracted seismograms (0.01–0.05 Hz, red traces) and compare to the seismograms expected from the observed pressure within that passband (black dashed traces). These two traces agree well with each other. This indicates the information of the band-limited velocity or displacement could be obtained from the bandpass-filtered pressure records, only in a few minutes from the focal time.

4 Conclusion

We developed a method to extract near-field seismograms from the OBP data inside the focal area. We applied the method to the near-field OBP data of the 2011 Tohoku-Oki earthquake to extract the ground motions inside the focal area, whereas the near-field seismograms during the Tohoku-Oki earthquake have never been reported yet. Our analysis successfully decomposed the OBP data into the dynamic pressure changes dominant in the first ~120 s and the subsequent hydrostatic pressure changes due to tsunamis and permanent seafloor deformation. The extracted seismograms suggested that two dominant energy releases occurred beneath the OBPs near the epicenter. We confirmed the validity of the extracted seismograms based on the numerical seismic wave propagation simulation. Because the bandpass filter to reduce the low-frequency hydrostatic components also reduces the low-frequency ground motion components, our inversion-based method is essential to appropriately extract the ground motion waveform including the low-frequency permanent offset components. The high-frequency pressure change signals in the near-field OBP should be utilized more widely, for geophysical research as well as real-time tsunami forecasting.

Data Availability Statement

The Supplementary Data Set is available at https://doi.org/10.5281/zenodo.4420394. The Supplementary Dataset S1 includes the results obtained by the inversion analysis, such as the amplitudes of the source functions (m_{ijk}), the NetCDF grid file of the sea-surface displacement, and the spatial and temporal configuration of the basis functions. The OBP data off Miyagi installed by Tohoku University are available in Data Set S2. The OBP data off Kamaishi were provided upon request to Earthquake Research Insititute, the University of Tokyo. The bathymetry data of GEBCO 2020 Grid (GEBCO Bathymetric Compilation Group 2020, 2020) are available at https://www.gebco.net/data_and_products/gridded_bathymetry_data/. The F-net onshore seismometer data are available at http://doi.org/10.17598/nied.0005. The numerical simulation of the P-SV seismic wave propagation was conducted by using OpenSWPC (Maeda et al., 2017) Version 5.0.2, available at https://doi.org/10.5281/zenodo.3712650. We used Seismic Analysis Code (SAC) software for data processing (Goldstein et al., 2003). Figures were prepared using Generic Mapping Tools Version 6 (GMT6) software (Wessel et al., 2019).

Acknowledgments

This study was financially supported by the research project "Research concerning Interaction between the Tokai, Tonankai, and Nankai Earthquakes" of Ministry of Education, Culture, Sports, Science and Technology (MEXT), Japan, and by Japan Society for the Promotion of Science (JSPS) KAKENHI Grant Numbers JP20244070, JP26000002, JP15K17752, JP19H00708, JP19H02409, 19H05596, JP19K04021, and JP19K14818. TK thanks Yoshihiro Ito of Kyoto University for fruitful comments. TK also thanks Naotaka Y. Chikasada, Hisahiko Kubo, and Osamu Sandanbata of National Research Institute for Earth Science and Disaster Resilience for insightful discussions. The installation and retrieval of the OBPs of Tohoku University were conducted via Research Vessel (*R/V*) *Keifu-maru* and *R/V Ryofu-maru* (Japan Meteorological Agency), Supply Vessels (*S/Vs*) *Kaiko* and *Kaiyu* (Offshore Operation Co., Ltd.) and *S/V Shinsei-maru* (Fukada Salvage Co., Ltd). The OBPs at P03, P07, P08, and P09 were recovered in September 2011 by using Remotely Operated Vehicle (ROV) *Hakuyo-3000* (Fukada Salvage Co., Ltd.) (Hino et al., 2012; Arai et al., 2013). TK also thanks the captains and crews of these vessels and the staff and technicians at ERI for their efforts for their operation. We thank the Editor Germán Prieto, the Associate Editor, and Prof. Thorne Lay and another anonymous reviewer for their constructive comments.

References

Abrahams, L. S., Dunham, E. M., Krenz, L., Saito, T., Gabriel, A.-A. (2020). Comparison of techniques for coupled earthquake and tsunami modeling [Conference presentation abstract]. AGU Fall Meeting 2020, Online. https://agu.confex.com/agu/fm20/webprogram/Paper761271.html

Aki, K. & Richards, P. G. (2002). *Quantitative seismology* (2nd ed.). Mill Valley, CA: University Science Books.

An, C., Cai, C., Zheng, Y., Meng, L., & Liu, P. (2017). Theoretical solution and applications of ocean bottom pressure induced by seismic seafloor motion. *Geophysical Research Letters*, *44*, 10272–10281. https://doi.org/10.1002/2017GL075137

Arai, K., Naruse, H., Miura, R., Kawamura, K., Hino, R., Ito, Y., Inazu, D., Yokokawa, M., Izumi, N., Murayama, M., & Kasaya, T. (2013). Tsunami-generated turbidity current of the 2011 Tohoku-Oki earthquake. *Geology*, *41*(11), 1195–1198. https://doi.org/10.1130/G34777.1

Baba, T., Hirata, K., Hori, T., & Sakaguchi, H. (2006). Offshore geodetic data conducive to the estimation of the afterslip distribution following the 2003 Tokachi-oki earthquake. *Earth and Planetary Science Letters*, *241*, 281–292. https://doi.org/10.1016/j.epsl.2005.10.019

Baba, T., Takahashi, N., Kaneda, Y., Ando, K., Matsuoka, D., & Kato, T. (2015). Parallel implementation of dispersive tsunami wave modeling with a nesting algorithm for the 2011 Tohoku tsunami. *Pure and Applied Geophysics*, *172*, 3455–3472. https://doi.org/10.1007/s00024-015-1049-2

Dettmer, J., Hawkins, R., Cummins, P. R., Hossen, J., Sambridge, M., Hino, R., & Inazu, D. (2016). Tsunami source uncertainty estimation : The 2011 Japan tsunami. *Journal of Geophysical Research: Solid EarthSolid Earth*, *121*, 4483–4505. https://doi.org/10.1002/2015JB012764

Filloux, J. H. (1982). Tsunami recorded on the open ocean floor. *Geophysical Research Letters*, *9*, 25–28. https://doi.org/10.1029/GL009I001P00025

Fujiwara, T., Kodaira, S., No, T., Kaiho, Y., Takahashi, N., & Kaneda, Y. (2011). The 2011 Tohoku-Oki earthquake: Displacement reaching the trench axis. *Science*, *334*, 1240. https://doi.org/10.1126/science.1211554

Fujiwara, T., dos Santos Ferreira, C., Bachmann, A. K., Strasser, M., Wefer, G., Sun, T., … Kodaira, S. (2017). Seafloor displacement after the 2011 Tohoku-oki earthquake in the northern Japan Trench examined by repeated bathymetric surveys. *Geophysical Research Letters*, *44*, 11,833-11,839. https://doi.org/10.1002/2017GL075839

Fukuyama, E., & Mikumo, T. (2007). Slip-weakening distance estimated at near-fault stations. *Geophysical Research Letters*, *34*, L09302. https://doi.org/10.1029/2006GL029203

Fukuyama, E., & Suzuki, W. (2016). Near-fault deformation and Dc″ during the 2016 Mw7.1 Kumamoto earthquake. *Earth, Planets and Space*, *68*, 194. https://doi.org/10.1186/s40623-016-0570-6

GEBCO Bathymetric Compilation Group 2020 (2020). *GEBCO 2020 Grid –a continuous terrain model of the global oceans and land* [Data set]. British Oceanographic Data Centre, National Oceanography Centre, Natural Environment Research Council, United Kingdom. https://doi.org/10/dtg3

Goldstein, P., Dodge, D. , Firpo, M., & Minner L. (2003). SAC2000: Signal processing and analysis tools for seismologists and engineers. In: W. H. K. Lee, H. Kanamori, P. C. Jennings, & C. Kisslinger (Eds.), *International Handbook of Earthquake and Engineering Seismology* (Vol. 81(B), pp. 1613–1614). London: Academic Press. https://doi.org/10.1016/S0074-6142(03)80284-X

Gusman, A. R., Tanioka, Y., Sakai, S., & Tsushima, H. (2012). Source model of the great 2011 Tohoku earthquake estimated from tsunami waveforms and crustal deformation data. *Earth and Planetary Science Letters*, *341–344*, 234–242. https://doi.org/10.1016/j.epsl.2012.06.006

Heidarzadeh, M. & Gusman A. R. (2018). Application of dense offshore tsunami observations from ocean bottom pressure gauges (OBPGs) for tsunami research and early warnings. In Durrani T., Wang W., Forbes S. (Eds.), *Geological Disaster Monitoring Based on Sensor Networks* (pp. 7-22). Singapore: Springer Singapore. https://doi.org/10.1007/978-981-13-0992-2_2

Hino, R. (2015). An overview of the Mw 9, 11 March 2011, Tohoku earthquake. *Summary of the Bulletin of the International Seismological Centre*, *48*, 100–132. https://doi.org/10.5281/zenodo.998789

Hino, R., Suzuki, S., Kubota, T., Ito, Y., & Fujimoto, H. (2012). Video image of seafloor near the epicenter of the 2011 Great Tohoku Earthquake. Abstract SSS39-P05 presented at JpGU Meeting 2012, Makuhari, Japan, May20–25, 2012. Retrieved October 15, 2020, from http://www2.jpgu.org/meeting/2012/session/PDF/S-SS39/SSS39-P05_e.pdf

Hino, R., Inazu, D., Ohta, Y., Ito, Y., Suzuki, S., Iinuma, T., … Kaneda, Y. (2014). Was the 2011 Tohoku-Oki earthquake preceded by aseismic preslip? Examination of seafloor vertical deformation data near the epicenter. *Marine Geophysical Research*, *35*, 181–190. https://doi.org/10.1007/s11001-013-9208-2

Hossen, M. J., Cummins, P. R., Dettmer, J., & Baba, T. (2015). Tsunami waveform inversion for sea surface displacement following the 2011 Tohoku earthquake: Importance of dispersion and source kinematics. *Journal of Geophysical Research: Solid Earth*, *120*, 6452–6473. https://doi.org/10.1002/2015JB011942

Ide, S., & Takeo, M. (1997). Determination of constitutive relations of fault slip based on seismic wave analysis. *Journal of Geophysical Research*, *102*(B12), 27,379–27,391. https://doi.org/10.1029/97JB02675

Iinuma, T., Hino, R., Kido, M., Inazu, D., Osada, Y., Ito, Y., … Miura, S. (2012). Coseismic slip distribution of the 2011 off the Pacific Coast of Tohoku Earthquake (M9.0) refined by means of seafloor geodetic data. *Journal of Geophysical Research*, *117*, B07409. https://doi.org/10.1029/2012JB009186

Ito, Y., Tsuji, T., Osada, Y., Kido, M., Inazu, D., Hayashi, Y., … Fujimoto, H. (2011). Frontal wedge deformation near the source region of the 2011 Tohoku-Oki earthquake. *Geophysical Research Letters*, *38*(15), L00G05. https://doi.org/10.1029/2011GL048355

Ito, Y., Webb, S. C., Kaneko, Y., Wallace, L. M., & Hino, R. (2020). Sea surface gravity waves excited by dynamic ground motions from large regional earthquakes. *Seismological Research Letters*. https://doi.org/10.1785/0220190267

Kajiura, K. (1963). The leading wave of a tsunami. *Bulletin of the Earthquake Research Institute*, *41*, 535–571.

Kanazawa, T., & Hasegawa, A. (1997). Ocean-bottom observatory for earthquakes and tsunami off Sanriku, north-eastern Japan using submarine cable. *Proceedings of International Workshop on Scientific Use of Submarine Cables*, 208–209.

Kaneko, Y., Fukuyama, E., & Hamling, I. J. (2017). Slip-weakening distance and energy budget inferred from near-fault ground deformation during the 2016 Mw7.8 Kaikōura earthquake. *Geophysical Research Letters*, *44*, 4765–4773. https://doi.org/10.1002/2017GL073681

Kido, M., Osada, Y., Fujimoto, H., Hino, R., & Ito, Y. (2011). Trench-normal variation in observed seafloor displacements associated with the 2011 Tohoku-Oki earthquake. *Geophysical Research Letters*, *38*, L24303. https://doi.org/10.1029/2011GL050057

Kodaira, S., Fujiwara, T., Fujie, G., Nakamura, Y., & Kanamatsu, T. (2020). Large coseismic slip to the trench during the 2011 Tohoku-Oki earthquake. *Annual Review of Earth and Planetary Sciences*, *48*, 321–343. https://doi.org/10.1146/annurev-earth-071719-055216

Koketsu, K., Miyake, H., Suzuki, H. (2012). Japan integrated velocity structure model version 1. In: Proceedings of the 15th world conference on earthquake engineering. Lisbon, Portugal, 24–28 September. Retrieved October 15, 2020, from https://www.iitk.ac.in/nicee/wcee/article/WCEE2012_1773.pdf

Kozdon, J. E., & Dunham, E. M. (2014). Constraining shallow slip and tsunami excitation in megathrust ruptures using seismic and ocean acoustic waves recorded on ocean-bottom sensor networks. *Earth and Planetary Science Letters*, *396*, 56–65. https://doi.org/10.1016/j.epsl.2014.04.001

Kubota, T., Hino, R., Inazu, D., Ito, Y., Iinuma, T., Ohta, Y., … Suzuki, K. (2017). Coseismic slip model of offshore moderate interplate earthquakes on March 9, 2011 in Tohoku using tsunami waveforms. *Earth and Planetary Science Letters*, *458*, 241–251. https://doi.org/10.1016/j.epsl.2016.10.047

Kubota, T., Saito, T., Suzuki, W., & Hino, R. (2017). Estimation of seismic centroid moment tensor using ocean bottom pressure gauges as seismometers. *Geophysical Research Letters*, *44*, 10907–10915. https://doi.org/10.1002/2017GL075386

Kubota, T., Saito, T., Ito, Y., Kaneko, Y., Wallace, L. M., Suzuki, S., … Henrys, S. (2018). Using tsunami waves reflected at the coast to improve offshore earthquake source parameters: application to the 2016 Mw 7.1 Te Araroa earthquake, New Zealand. *Journal of Geophysical Research: Solid Earth*, *123*, 8767–8779. https://doi.org/10.1029/2018JB015832

Kubota, T., Saito, T., Chikasada, N. Y. & Suzuki, W. (2020). Ultra-broadband seismic and tsunami wave observation of high-sampling ocean-bottom pressure gauge covering periods from seconds to hours. *Earth and Space Science*, *7*, e2020EA001197. https://doi.org/10.1029/2020EA001197

Lay, T. (2018). A review of the rupture characteristics of the 2011 Tohoku-oki Mw 9.1 earthquake. *Tectonophysics*, *733*, 4–36. https://doi.org/10.1016/j.tecto.2017.09.022

Lay, T., Ammon, C. J., Kanamori, H., Xue, L., & Kim, M. J. (2011). Possible large near-trench slip during the 2011 Mw 9.0 off the Pacific coast of Tohoku Earthquake. *Earth, Planets and Space*, *63*, 687–692. https://doi.org/10.5047/eps.2011.05.033

Lay, T., Kanamori, H., Ammon, C. J., Koper, K. D., Hutko, A. R., Ye, L., … Rushing, T. M. (2012). Depth-varying rupture properties of subduction zone megathrust faults. *Journal of Geophysical Research*, *117*, B04311. https://doi.org/10.1029/2011JB009133

Lotto, G. C., & Dunham, E. M. (2015). High-order finite difference modeling of tsunami generation in a compressible ocean from offshore earthquakes. *Computational Geosciences*, *19*(2), 327–340. https://doi.org/10.1007/s10596-015-9472-0

Lotto, G. C., Jeppson, T. N., & Dunham, E. M. (2019). Fully coupled simulations of megathrust earthquakes and tsunamis in the Japan Trench, Nankai Trough, and Cascadia Subduction Zone. *Pure and Applied Geophysics*. https://doi.org/10.1007/s00024-018-1990-y

Ma, S., & Nie, S. (2019). Dynamic wedge failure and along-arc variations of tsunamigenesis in the Japan Trench margin. *Geophysical Research Letters*, *46*, 8782–8790. https://doi.org/10.1029/2019GL083148

Madariaga, R., Ruiz, S., Rivera, E., Leyton, F., & Baez, J. C. (2019). Near-field spectra of large earthquakes. *Pure and Applied Geophysics*, *176*, 983–1001. https://doi.org/10.1007/s00024-018-1983-x

Maeda, T., Furumura, T., Sakai, S., & Shinohara, M. (2011). Significant tsunami observed at ocean-bottom pressure gauges during the 2011 off the Pacific coast of Tohoku Earthquake. *Earth, Planets and Space*, *63*, 803–808. https://doi.org/10.5047/eps.2011.06.005

Maeda, T., Takemura, S., & Furumura, T. (2017). OpenSWPC: An open-source integrated parallel simulation code for modeling seismic wave propagation in 3D heterogeneous viscoelastic media 4. Seismology. *Earth, Planets and Space*, *69*, 102. https://doi.org/10.1186/s40623-017-0687-2

Maeda, T., Saito, T., & Baba, T. (2020). *OpenSWPC + JAGURS: Towards waves-of-all-kinds simulation associated with significant earthquakes* [Conference presentation abstract]. JpGU-AGU Joint Meeting 2020, Online. https://confit.atlas.jp/guide/event/jpgu2020/subject/SCG70-07/detail

Matsumoto, H., Inoue, S., & Ohmachi, T. (2012). Dynamic response of bottom water pressure due to the 2011 Tohoku earthquake. *Journal of Disaster Research*, *7*, 468–475. https://doi.org/10.20965/jdr.2012.p0468

Matsumoto, H., Nosov, M. A., Kolesov, S. V., & Kaneda, Y. (2017). Analysis of pressure and acceleration signals from the 2011 Tohoku earthquake observed by the DONET seafloor network. *Journal of Disaster Research*, *12*, 163–175. https://doi.org/10.20965/jdr.2017.p0163

Matsumoto, K., Takanezawa, T., & Ooe, M. (2000). Ocean tide models developed by assimilating TOPEX/POSEIDON altimeter data into hydrodynamical model: A global model and a regional model around Japan. *Journal of Oceanography*, *56*, 567–581. https://doi.org/10.1023/A:1011157212596

Melgar, D., & Hayes, G. P. (2019). Characterizing large earthquakes before rupture is complete. *Science Advances*, *5*, eaav2032. https://doi.org/10.1126/sciadv.aav2032

Mikada, H., Mitsuzawa, K., Matsumoto, H., Watanabe, T., Morita, S., Otsuka, R., … Suyehiro, K. (2006). New discoveries in dynamics of an M8 earthquake-phenomena and their implications from the 2003 Tokachi-oki earthquake using a long term monitoring cabled observatory. *Tectonophysics*, *426*, 95–105. https://doi.org/10.1016/j.tecto.2006.02.021

Mikumo, T., Olsen, K. B., Fukuyama, E., & Yagi, Y. (2003). Stress-breakdown time and slip-weakening distance inferred from slip-velocity functions on earthquake faults. *Bulletin of the Seismological Society of America*, *93*, 264–282. https://doi.org/10.1785/0120020082

Mizutani, A., Yomogida, K., & Tanioka, Y. (2020). Early tsunami detection with near-fault ocean-bottom pressure gauge records based on the comparison with seismic data at common sites Key Points : *Journal of Geophysical Research: Oceans*, *125*, e2020JC016275. https://doi.org/10.1029/2020JC016275

Nakamura, T., & Hayashimoto, N. (2019). Rotation motions of cabled ocean-bottom seismic stations during the 2011 Tohoku earthquake and their effects on magnitude estimation for early warnings. *Geophysical Journal International*, *216*, 1413–1427. https://doi.org/10.1093/gji/ggy502

Nemoto, M., Yokota, T., Takase, S., & Imamura, F. (2019). Re-examination of the tsunami source model of the 2011 off Pacific coast of Tohoku earthquake –an estimation fully using available data of tsunami-related observation–. *Journal of Japan Association ofr Earthquake Engineering*, *19*, 2_25–2_41 (in Japanese with English abstract). https://doi.org/10.5610/jaee.19.2_25

Nosov, M. A., & Kolesov, S. V. (2007). Elastic oscillations of water column in the 2003 Tokachi-oki tsunami source: in-situ measurements and 3-D numerical modelling. *Natural Hazards and Earth System Science*, *7*, 243–249. https://doi.org/10.5194/nhess-7-243-2007

Okada, Y., Kasahara, K., Hori, S., Obara, K., Sekiguchi, S., Fujiwara, H., & Yamamoto, A. (2004). Recent progress of seismic observation networks in Japan - Hi-net, F-net, K-NET and KiK-net. *Earth, Planets and Space*, *56*, xv–xxviii. https://doi.org/10.1186/BF03353076

Saito, T. (2013). Dynamic tsunami generation due to sea-bottom deformation: Analytical representation based on linear potential theory. *Earth, Planets and Space*, *65*, 1411–1423. https://doi.org/10.5047/eps.2013.07.004

Saito, T. (2017). Tsunami generation: validity and limitations of conventional theories. *Geophysical Journal International*, *210*, 1888–1900. https://doi.org/10.1093/gji/ggx275

Saito, T. (2019). *Tsunami Generation and Propagation*. Tokyo: Springer Japan. https://doi.org/10.1007/978-4-431-56850-6

Saito, T., & Furumura, T. (2009). Three-dimensional tsunami generation simulation due to sea-bottom deformation and its interpretation based on the linear theory. *Geophysical Journal International*, *178*, 877–888. https://doi.org/10.1111/j.1365-246X.2009.04206.x

Saito, T., & Tsushima, H. (2016). Synthesizing ocean bottom pressure records including seismic wave and tsunami contributions: Toward realistic tests of monitoring systems. *Journal of Geophysical Research: Solid Earth*, *121*, 8175–8195. https://doi.org/10.1002/2016JB013195

Saito, T., & Kubota, T. (2020). Tsunami modeling for the deep sea and inside focal areas. *Annual Review of Earth and Planetary Sciences*, *48*, 121–145. https://doi.org/10.1146/annurev-earth-071719-054845

Saito, T., Ito, Y., Inazu, D., & Hino, R. (2011). Tsunami source of the 2011 Tohoku-Oki earthquake, Japan: Inversion analysis based on dispersive tsunami simulations. *Geophysical Research Letters*, *38*, L00G19. https://doi.org/10.1029/2011GL049089

Saito, T., Baba, T., Inazu, D., Takemura, S., & Fukuyama, E. (2019). Synthesizing sea surface height change including seismic waves and tsunami using a dynamic rupture scenario of anticipated Nankai trough earthquakes. *Tectonophysics*, *769*, 228166. https://doi.org/10.1016/j.tecto.2019.228166

Satake, K., Fujii, Y., Harada, T., & Namegaya, Y. (2013). Time and space distribution of coseismic slip of the 2011 Tohoku earthquake as inferred from Tsunami waveform data. *Bulletin of the Seismological Society of America*, *103*(2B), 1473–1492. https://doi.org/10.1785/0120120122

Sato, M., Ishikawa, T., Ujihara, N., Yoshida, S., Fujita, M., Mochizuki, M., & Asada, A. (2011). Displacement above the hypocenter of the 2011 Tohoku- Oki Earthquake. *Science*, *332*, 1395. https://doi.org/10.1126/science.1207401

Suzuki, K., Hino, R., Ito, Y., Yamamoto, Y., Suzuki, S., Fujimoto, H., … Kaneda, Y. (2012). Seismicity near the hypocenter of the 2011 off the Pacific coast of Tohoku earthquake deduced by using ocean bottom seismographic data. *Earth, Planets and Space*, *64*, 1125–1135. https://doi.org/10.5047/eps.2012.04.010

Takagi, R., Uchida, N., Nakayama, T., Azuma, R., Ishigami, A., Okada, T., … Shiomi, K. (2019). Estimation of the orientations of the S-net cabled ocean-bottom sensors. *Seismological Research Letters*, *90*, 2175–2187. https://doi.org/10.1785/0220190093

Tsushima, H., Hirata, K., Hayashi, Y., Tanioka, Y., Kimura, K., Sakai, S., … Maeda, K. (2011). Near-field tsunami forecasting using offshore tsunami data from the 2011 off the Pacific coast of Tohoku Earthquake. *Earth, Planets and Space*, *63*(7), 821–826. https://doi.org/10.5047/eps.2011.06.052

Tsushima, H., Hino, R., Tanioka, Y., Imamura, F., & Fujimoto, H. (2012). Tsunami waveform inversion incorporating permanent seafloor deformation and its application to tsunami forecasting. *Journal of Geophysical Research*, *117*, B03311. https://doi.org/10.1029/2011JB008877

Yamazaki, Y., Cheung, K. F., & Lay, T. (2018). A self-consistent fault slip model for the 2011 Tohoku earthquake and tsunami. *Journal of Geophysical Research: Solid Earth*, *123*(2), 1435–1458. https://doi.org/10.1002/2017JB014749

Vigny, C., Socquet, A., Peyrat, S., Ruegg, J.-C., Métois, M., Madariaga, R., … Kendrick, E. (2011). The 2010 Mw 8.8 Maule Megathrust Earthquake of Central Chile, Monitored by GPS. *Science*, *332*, 1417–1422. https://doi.org/10.1126/science.1204132

Wang, K., Sun, T., Brown, L., Hino, R., Tomita, F., Kido, M., … Fujiwara, T. (2018). Learning from crustal deformation associated with the M9 2011 Tohoku-oki earthquake. *Geosphere*, *14*, 1–20. https://doi.org/10.1130/GES01531.1

Webb, S. C. (1998). Broadband seismology and noise under the ocean. *Reviews of Geophysics*, *36*, 105–142. https://doi.org/10.1029/97RG02287

Webb, S. C., & Nooner, S. L. (2016). High-resolution seafloor absolute pressure gauge measurements using a better counting method. *Journal of Atmospheric and Oceanic Technology*, *33*, 1859–1874. https://doi.org/10.1175/JTECH-D-15-0114.1

Wessel, P., Luis, J. F., Uieda, L., Scharroo, R., Wobbe, F., Smith, W. H. F., & Tian, D. (2019). The Generic Mapping Tools Version 6. *Geochemistry, Geophysics, Geosystems*, *20*, 5556–5564. https://doi.org/10.1029/2019GC008515

Geophysical Research Letters

Supporting Information for

Extracting near-field seismogram from ocean-bottom pressure gauge inside the focal area: application to the 2011 Mw 9.1 Tohoku-Oki earthquake

T. Kubota[1], T. Saito[1], H. Tsushima[2], R. Hino[3], Y. Ohta[3], S. Suzuki[3], D. Inazu[4]

[1] National Research Institute for Earth Science and Disaster Resilience, Tsukuba, Japan
[2] Meteorological Research Institute, Japan Meteorological Agency, Tsukuba, Japan
[3] Graduate School of Science, Tohoku University, Sendai, Japan
[4] Department of Marine Resources and Energy, Tokyo University of Marine Science and Technology, Tokyo, Japan

Contents of this file

Additional Supporting Information (Files uploaded separately)

Datasets S1 contains the results obtained by the analysis in this study, such as the spatial and temporal configuration of the basis functions. Dataset S2 contains the OBP data used in this study.

Introduction

Text S1 describes the detail for the OBP instruments used in this study. Procedure for calculating the Green's function and for the inversion analysis is explained in Text S2. In Text S3, the procedure of the P-SV seismic wave simulation is shown. Calculation of the hydrostatic and dynamic pressure changes from the inversion result is shown in Figure S1. Figures S2 and S3 show the spatial distribution of the total displacement and temporal evolution of the displacement, respectively. Comparison of the amplitude spectra at GJT3 is shown in Figure S4. Figure S5 is the comparison of the observed pressure pressure and the simulated displacement. Figure S6 compares the seismograms obtained by this study and those expected from the bandpass filter and Figure S7 compares the bandpass-filtered seismograms. The station list is shown in Table S1.

Text S1.

This text describes the detail of the OBP instruments. We use seven OBPs installed off Miyagi by Tohoku University (green inverted triangles in Figure 1a), which utilize Paroscientific Digiquartz precise quartz pressure sensors, 8B7000 series (Hino et al., 2014). We also use two cabled OBPs installed off Iwate by the Earthquake Research Institute (ERI), the University of Tokyo (orange inverted triangles), which use the quartz pressure sensor manufactured by Hewlett-Packard Inc. (Kanazawa & Hasegawa, 1997; Maeda et al., 2011). Although the frequency response of a quartz pressure sensor generally depends on the counting method of the quartz oscillation, the response of the quartz pressure sensor is typically flat at lower frequency band of < ~1 Hz regardless of its counting method (Webb & Nooner, 2016). Station locations are listed in Table S1.

Text S2.

This text shows the further detail of the calculation of the Green's function and the inversion analysis. We suppose the x- and y-directions are along the trench-normal and trench-parallel directions, respectively (i.e., azimuth of x-direction is 105°). We distribute the spatial basis function $U_{z,ij}$ (Eq. (6)) in an area of 220 km × 270 km (gray dots in Figure 1a). This is determined based on the spatial extent of the initial sea-surface height (i.e., tsunami source) derived by the previous study (Saito et al., 2011). We suppose the elliptical-shaped unit sources to be L_x = 20 km and L_y = 60 km, and that each of them overlaps with their adjacent ones at horizontal intervals of $\Delta x = L_x/2$ and $\Delta y = L_y/2$ (inset of Figure 1a). These horizontal sizes and spatial intervals are also determined based on the spatial extent of the initial tsunami height obtained by the analysis of Saito et al. (2011), in order to resolve the tsunami height with the spatial scale of a few tens of km. Total number of the unit sources in the space domain is N_x = 21 and N_y = 17 along the x- and y-direction, respectively (total number of the unit sources in the space domain is $N_x \times N_y$ = 357). We also distribute the temporal basis functions, τ_k, in time domain, during the first 120 s from the origin time, with the temporal interval of $\Delta t = T_\mathrm{d}/2$ = 5 s (inset of Figure 1a). In other words, the parameter t_k, the beginning of the time function τ_k, is assumed as $t_k = (k\text{-}1)\Delta t$, $1 \le k \le N_t$. N_t = 23 is the total number of the basis functions in time domain. This temporal basis function has a sine-type shape (Eq. (7), e.g., Maeda et al., 2017) and the duration of the displacement is assumed as T_d = 10 s. The duration and the temporal interval are determined in order to appropriately reproduce the signals with the frequency lower than the cutoff period of the lowpass filter, 0.05 Hz (period of 20 s).

To calculate the hydrostatic Green's function, tsunami height is numerically simulated from the initial tsunami height distribution using the linear dispersive tsunami equation (e.g., Saito et al., 2019) with a time step interval of 1 s. We use the bathymetry data of GEBCO Bathymetric Compilation Group (2020), decimating to a spatial grid interval of 2 km. The input sea-surface height for the tsunami calculation is calculated from the unit seafloor displacement $U_{z,ij}(x, y)$ with the water wave theory assuming a constant depth of 6 km (Kajiura, 1963). The dynamic Green's functions are also calculated based on Eq. (3), using the seawater depth h_0 for each station (Table S1). After the calculation of the Green's functions, the same filter as applied to the observation is also applied to the Green's functions.

In the inversion, we impose the constraints of the spatial smoothing (Baba et al., 2006) and spatial damping. The weights of each constraint are determined based on trial and error. The deformations are allowed to begin at t = 0 s. We use 3600-s time windows for the OBPs of Tohoku University and 1800-s for the OBPs of ERI for the inversion.

Text S3.

This text shows the detail of the numerical simulation of the two-dimensional P-SV seismic wave propagation (Figure 4). We solve the equations for the elastic body using the finite difference method (Maeda et al., 2017). We assume the vertical cross-section passing through GJT3 along the trench-normal direction (azimuth = 105°) from the extended Japan Integrated Velocity Structure Model (Koketsu et al., 2012) with a grid interval of 0.2 km (top panel in Figure 4). We distribute point sources along the plate boundary. We assume their rupture begins at the same time and the source durations are 4 s. After the calculation, we apply lowpass filters with different cutoffs to compare the pressure ($p = -\sigma_{zz}$, red traces) and the pressure-converted vertical acceleration ($\rho_0 h_0 \mathrm{d}^2 u_z/\mathrm{d}t^2$, blue traces) at the station GJT3. The amplitudes in each subfigure are normalized so that the maximum amplitude of the traces without the lowpass filter (left top subfigure in Figure 4) takes 1.

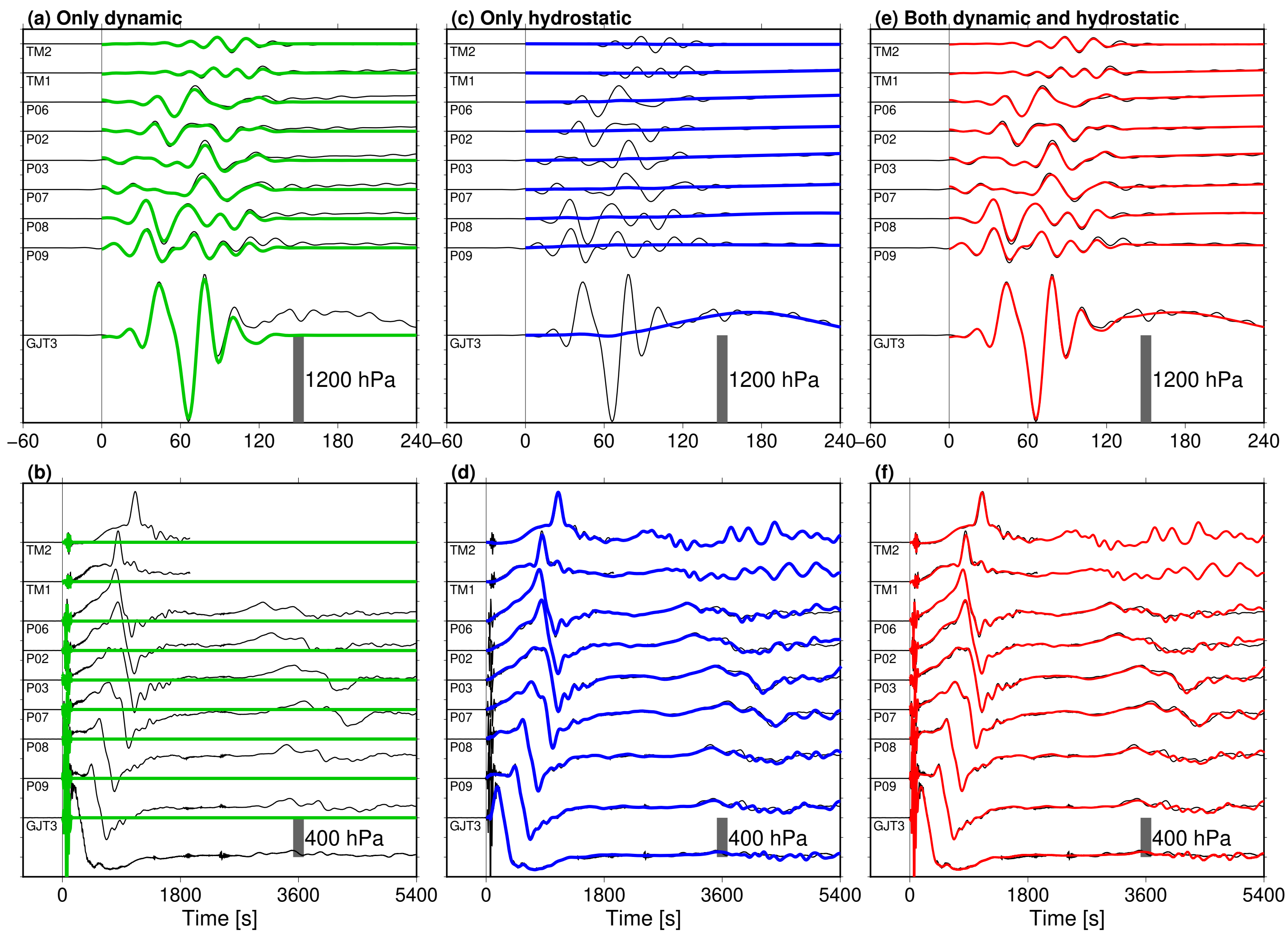

Figure S1. Comparison between the observed pressure waveforms (black) with the simulated waveforms, for (a,b) dynamic (green), (c, d) hydrostatic (blue), and (e,f) both pressure changes. The lowpass filter with a cutoff of 0.05 Hz is applied.

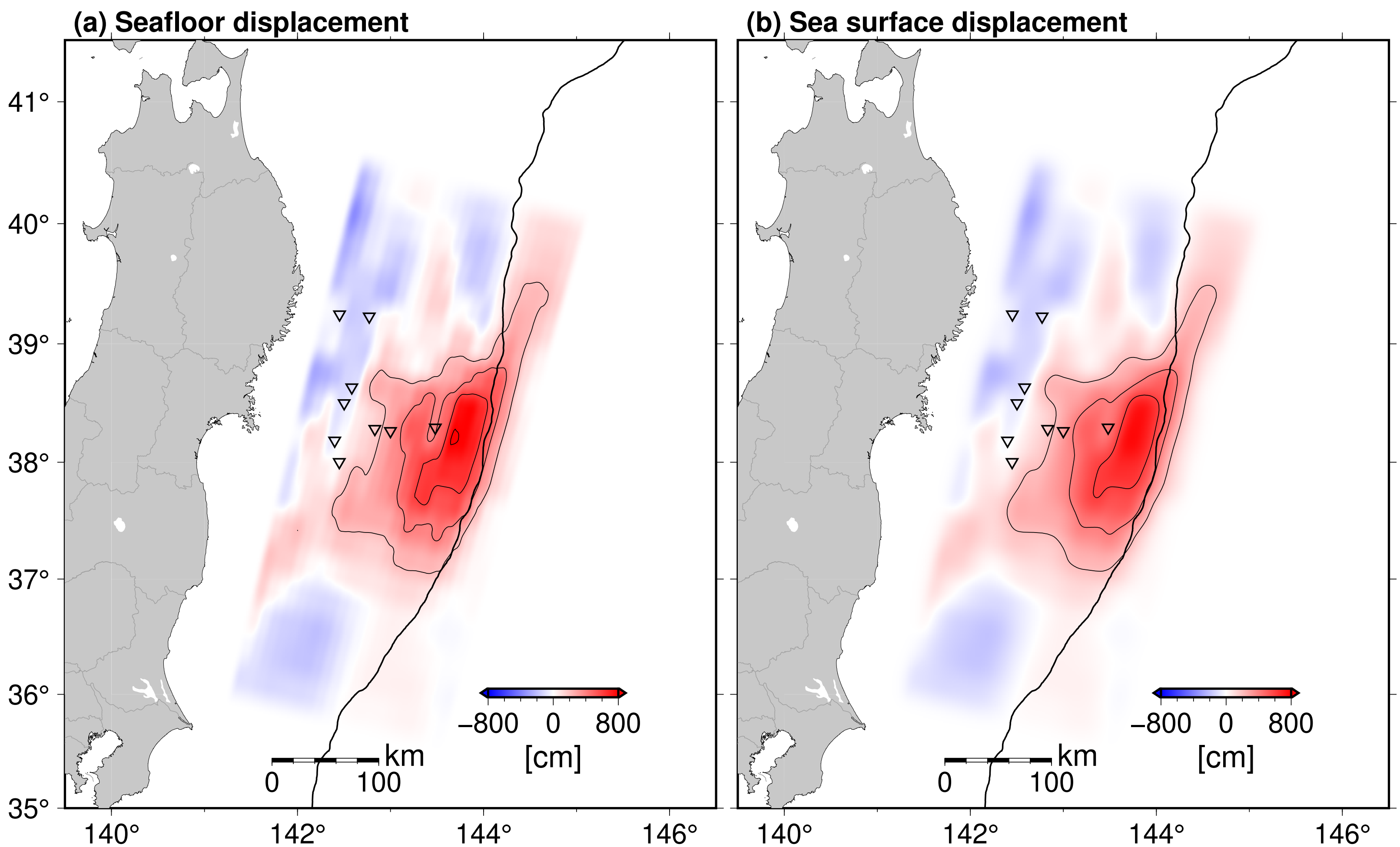

Figure S2. The spatial distribution of (a) the seafloor and (b) the sea-surface height obtained by the inversion analysis. The contour interval is 2 m.

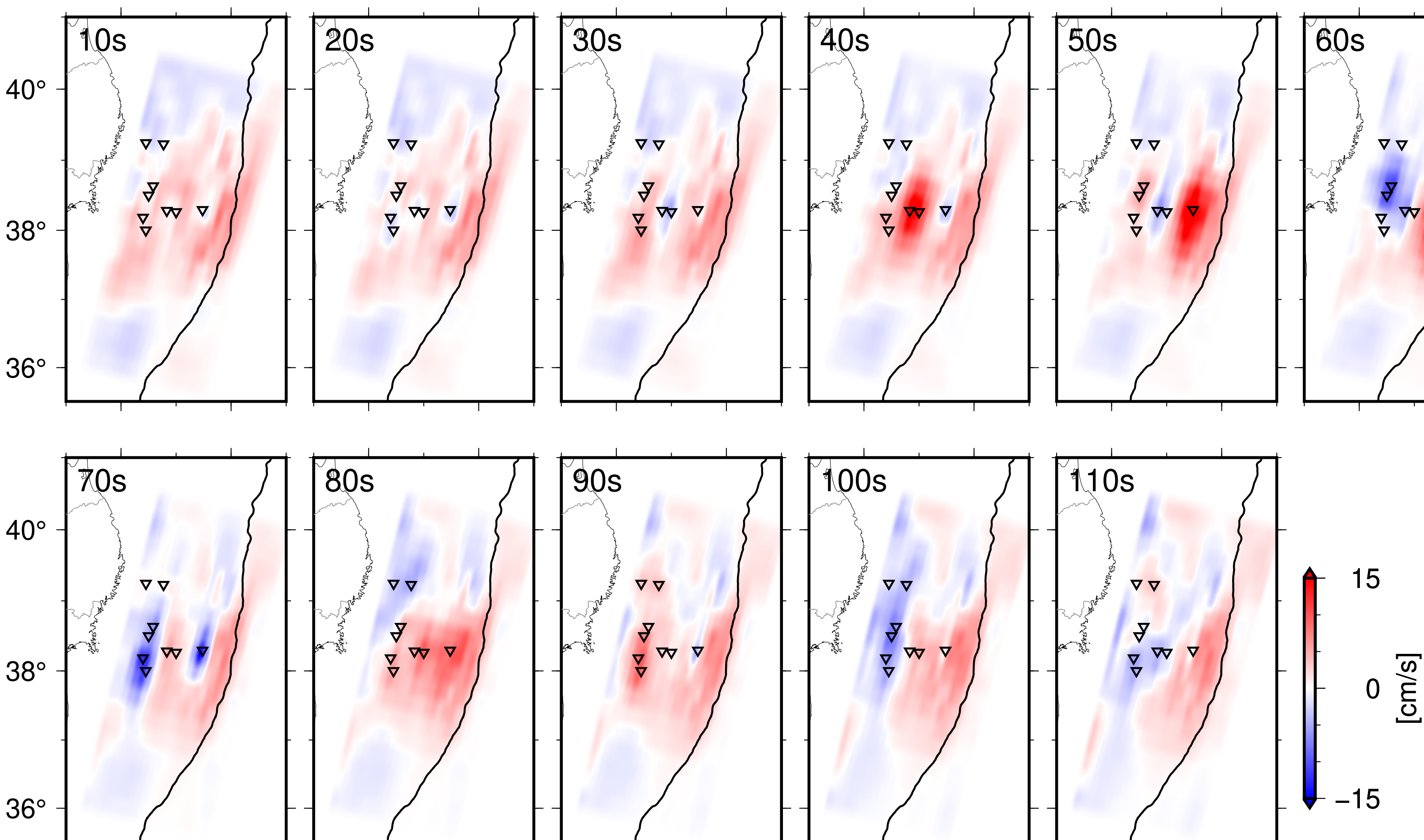

Figure S3. The temporal evolution of the seafloor displacement rate obtained by the inversion analysis.

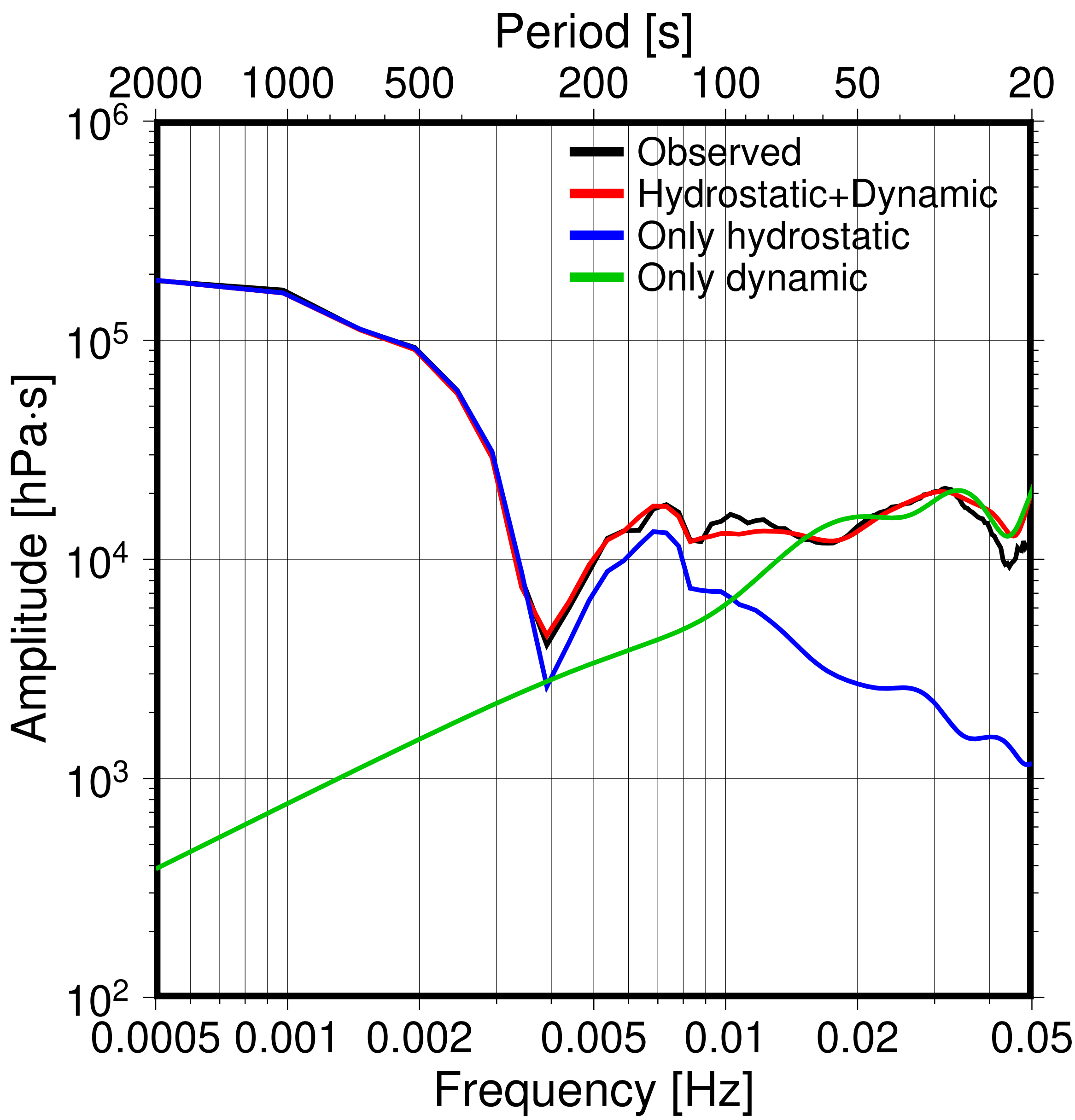

Figure S4. Comparison of spectral amplitudes at GJT3 between the observed one (black) and calculated ones; red: both hydrostatic and dynamic, blue: only hydrostatic, green: only dynamic pressure changes. The time window of 2048 s from the origin time is used for the spectral calculation.

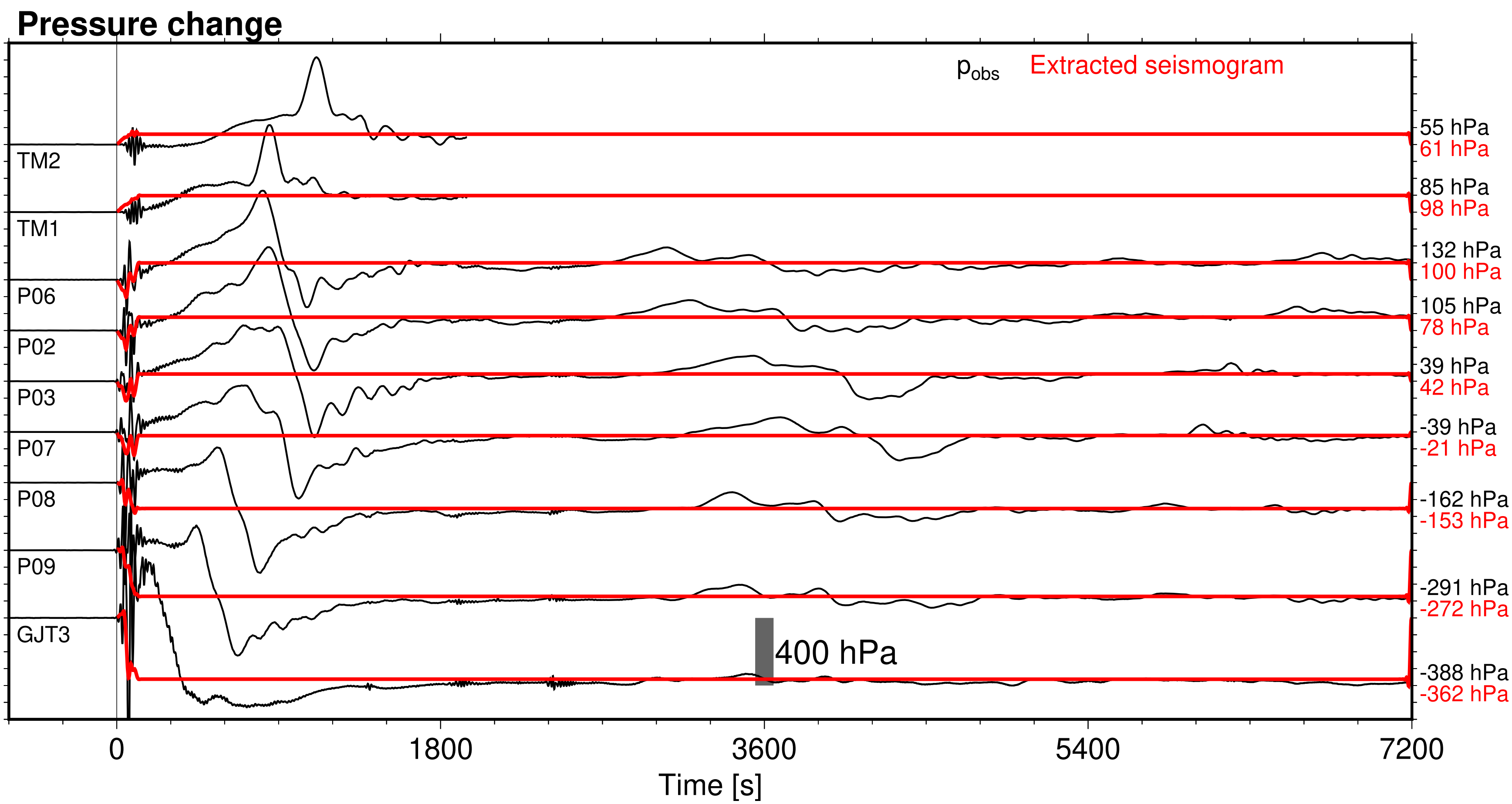

Figure S5. Comparison of the observed pressure time series (black) and those expected from the extracted displacement (red) for two hours from the origin time. The final pressure offsets, calculated by averaging the last 600 s time window, are also shown.

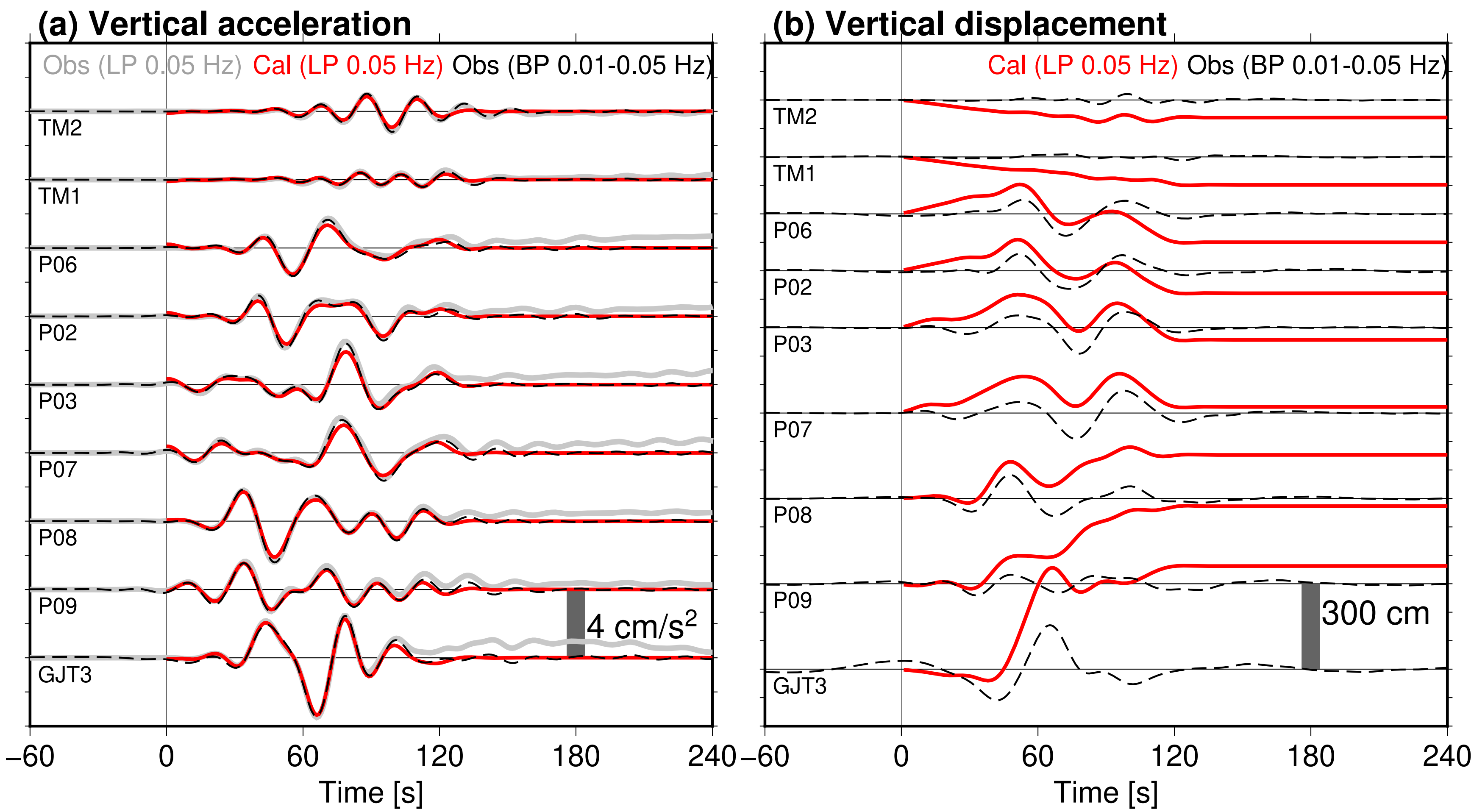

Figure S6. Comparison between the extracted seismograms (red), and the lowpass-filtered (0.05 Hz, gray) and the bandpass-filtered (0.01–0.05 Hz, black dashed) waveforms, for (a) vertical acceleration and (b) vertical displacement.

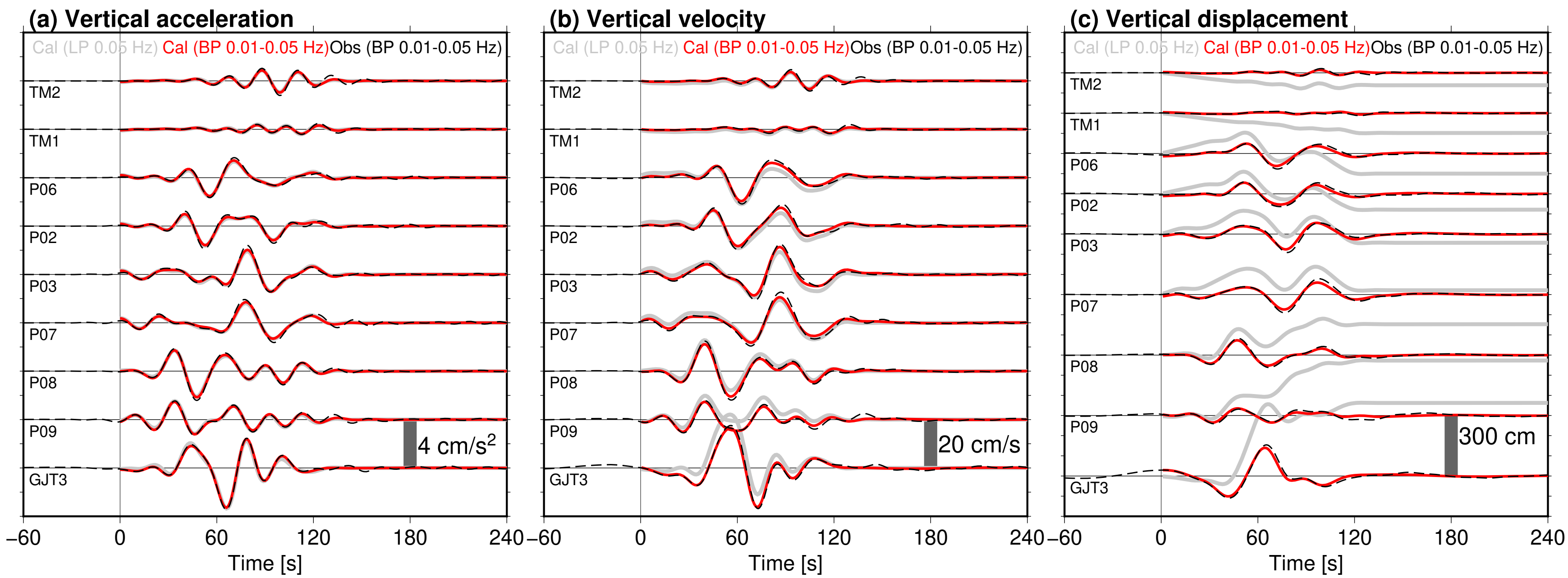

Figure S7. Time series of the extracted vertical seismograms based on the inversion with the bandpass-filter (0.05–0.01 Hz, red traces), for (a) acceleration, (b) velocity and (c) displacement. Gray traces are the extracted vertical seismograms with the lowpass filter (0.05 Hz). Black dashed traces are the bandpass-filtered observed data (0.01–0.05 Hz).

Table S1. List of the stations used in this study.[a]

Station	Latitude [°N]	Longitude [°E]	Depth [m]	Inversion time window [s]	Agency
GJT3	38.2945	143.4814	3293	0 – 3600	Tohoku University
P02	38.5002	142.5016	1104	0 – 3600	Tohoku University
P03	38.1834	142.3998	1052	0 – 3600	Tohoku University
P06	38.6340	142.5838	1254	0 – 3600	Tohoku University
P07	38.0003	142.4488	1059	0 – 3600	Tohoku University
P08	38.2855	142.8330	1418	0 – 3600	Tohoku University
P09	38.2659	143.0006	1556	0 – 3600	Tohoku University
TM1	39.2312	142.7684	1618	0 – 1800	ERI
TM2	39.2489	142.4412	1013	0 – 1800	ERI

[a]All data were resampled to 1 Hz after the filtering process.